Indian Journal of Chemical Technology
Vol. 32, November 2025, pp. 710-722
DOI: 10.56042/ijct.v32i6.21749

Enhanced photocatalytic and antibacterial performance of ZnO and ZnS synthesized using natural fuel: Influence of green synthesis, particle size, and morphology

J. Karthick[1] & V. S. Sreenivasan[2] *

[1]Department of Mechanical Engineering, PET Engineering College, Vallioor, Tamil Nadu, India
[2]Department of Mechanical Engineering, Sri Krishna College of Technology, Coimbatore, Tamil Nadu, India
*E-mail: vssreenivasan@ymail.com

Received 18 July 2025; accepted 31 October 2025

This study reveals the eco-friendly synthesis of zinc oxide (ZnO) and zinc sulfide (ZnS) nanoparticles using aqueous neem flower (*Azadirachta indi*ca) extract as a green reducing and stabilizing agent. The nanoparticles have been characterized by XRD, FTIR, UV-visible spectroscopy, FESEM, EDX, and DLS techniques. Structural and morphological characterization confirmed the efficacious development of hexagonal ZnO and cubic ZnS phases, with crystallite sizes of 40.42 nm and 16.24 nm, respectively. FTIR analysis revealed the existence of phytochemical capping groups, indicating the role of neem extract in nanoparticle stabilization. DLS analysis further supported these result**s**, which showed a broader size distribution for ZnO (85.69 nm) and a narrower, polydisperse distribution for ZnS (24.93 nm). The photocatalytic performance has been examined under sunlight for degradation of acrylic orange and alizarin red S dyes. ZnO exhibited superior photocatalytic performance, degrading 95.72% of acrylic orange and 92.37% of alizarin red S**,** with higher rate constants than ZnS**,** and maintaining over 88% stability after five reuse cycles. Additionally, both nanoparticles demonstrated effective antibacterial activity, with ZnO showing larger inhibition zones against *S. aureus* and *E. coli,* likely due to its higher reactive oxygen species generation and more favourable morphology.

Keywords: Antibacterial, Dye degradation, Green synthesis, Neem flower extract, Zinc oxide, Zinc sulfide

Introduction

Water pollution has become an alarming global issue, primarily driven by rapid industrialization and uncontrolled discharge of untreated effluents into natural water bodies. Among the numerous pollutants, synthetic dyes used expansively in textile, leather, and plastic industries pose a severe health threat due to their persistent, non-biodegradable, and cancer-causing nature[1-2]. These dyes are designed to resist fading and degradation, making them difficult to remove through conventional treatment methods. Two such dyes, alizarin red S, an anthraquinone-based dye, and acrylic orange**,** an azo dye, are commonly released in large volumes from industrial processes. Their complex aromatic molecular structures confer high chemical stability and resistance to natural decomposition, allowing them to persist in aquatic ecosystems, where they hinder photosynthesis, lower oxygen content, and pose toxicity risks to flora, fauna, and even humans[3-4]. These issues necessitate the advance of effective, low-cost, and ecologically benign techniques for the breakdown and elimination of synthetic dyes from effluent. One promising strategy to tackle this challenge is using nanotechnology, specifically by applying metal and metal oxide nanoparticles (NPs) that exhibit good catalytic and antimicrobial properties[5-6].

Conventional approaches for synthesizing such NPs habitually comprise toxic precursors, high temperatures, and expensive equipment, raising apprehensions about human safety[7-8]. Among various biological agents, plant extracts, particularly from medicinal plants, offer a rich cause of bioactive complexes that can act as natural capping, reducing and stabilizing agents. These phytochemicals facilitate NP formation under mild conditions and impart additional biological functionality, making the NPs more compatible for applications in environmental and biomedical fields.

Using neem flower extract as a green route for (*Azadirachta indica*) NP synthesis offers significant advantages. Neem is a widely recognized medicinal plant, valued for its antioxidant, antimicrobial and anti-inflammatory activities. Its flowers are rich in flavonoids, polyphenols, tannins, and other secondary metabolites. Utilizing neem flowers makes the synthesis process eco-friendly and capable of yielding NPs with enhanced functional properties[9-10]. The ZnO and ZnS are II-VI semiconductors with wide bandgaps, making them extremely operative under UV light for

photocatalytic processes. ZnO NPs are widely recognized for their strong photocatalytic activity, high exciton binding energy, and intrinsic antibacterial properties. They generate reactive oxygen species (ROS) under light irradiation, which leads to the oxidative breakdown of complex dye molecules and microbial cell structures[11-12]. Similarly, ZnS NPs possess strong luminescent and photocatalytic capabilities and have shown promise in degrading organic pollutants and inhibiting bacterial growth. Their biocompatibility and relatively low toxicity further expand their applicability in environmental and biomedical sectors[13,14]. The photocatalytic degradation of anionic dye (alizarin red S) and cationic dye (acrylic orange) by ZnO and ZnS NPs synthesized via neem flower extract is particularly relevant due to the structural complexity and environmental persistence of these dyes. Alizarin red S, known for its use in the textile and biomedical staining industries, contains anthraquinone groups that contribute to its high chemical stability and resistance to biodegradation. On the other hand, acrylic orange, an azo dye, includes one or more azo bonds (-N=N-) that break down into aromatic amines, some of which are potential carcinogens. Conventional dye amputation approaches such as coagulation, and membrane filtration are often inefficient, costly, or generate secondary pollutants. Photocatalysis using nanoparticles presents a more sustainable and effective method, enabling the comprehensive mineralization of dyes into innocuous end goods like CO_2 and water without producing hazardous byproducts[15-16].

Benefits of ZnO and ZnS NPs extend beyond their photocatalytic activity to include their antimicrobial characteristics. It is crucial to develop alternative antimicrobial techniques due to the rise of drug-resistant bacterial strains caused by the abuse of traditional antibiotics. Green-synthesized NPs have shown potent antibacterial activity against a range of bacterial strains, including gram-positive and gram-negative varieties. ZnO and ZnS NPs cause oxidative stress in bacteria by breaking down their cell walls and releasing metal ions that disrupt important cellular processes. This complex action mechanism of these NPs makes their use in antibacterial applications more plausible and lessens the chances of bacteria acquiring resistance[17-18].

The materials used in this study include zinc acetate and zinc sulfate as precursors for ZnO and ZnS NPs, respectively. The neem flower extract is a natural stabilizing and reducing agent, eliminating the need for toxic surfactants or chemical reducers[19-20]. The synthesis is carried out under ambient conditions, reinforcing the sustainability and scalability of the process. The photocatalytic experiments involve the degradation of alizarin red S and acrylic orange under simulated sunlight, with dye concentrations monitored spectrophotometrically[20-21]. Antibacterial studies use standard good diffusion and MIC (Minimum Inhibitory Concentration) methods against representative bacterial strains like *Escherichia coli* and *Staphylococcus aureus*. The novelty of using neem flower extract for ZnO and ZnS NPs lies in its dual benefits, providing a clean, biocompatible synthesis route and enhancing the functional properties of the NPs through phytochemical capping[21-22].This work sets the stage for future development and large-scale application of green-synthesized nanoparticles in water treatment through eco-friendly synthesis, detailed characterization, and performance evaluation.

Experimental Section

The materials used for the whole process were *Azadirachta indica* flowers, distilled water, ethanol, Whatman No.1 filter paper, zinc acetate dihydrate, zinc chloride, sodium sulfide, mortar, and pestle. alizarin red S (anionic dye) and acrylic orange (cationic dye), bacterial strains (*Escherichia coli* and *Staphylococcus aureus)*, Streptomycin (S25), Muller Hinton Agar (MHA), Nutrient broth.

Preparation of neem flower extract

Fresh neem (*Azadirachta indica*) flowers were collected from healthy neem trees which is shade-dried at apartment temperature for 5 days. Once completely dried, the flowers were finely powdered using a clean grinder. For the extract preparation, 10 g of the neem flower powder was mixed with 130 mL of distilled water and heated at 70°C for about 30 min with continuous stirring. This process facilitates the release of polyphenols, terpenoids, and tannins into the aqueous medium. After heating, the mixture was cooled to ambient temperature and filtered for producing a clear, pale-yellow extract.

Synthesis of ZnO NPs

ZnO NPs were synthesized by a green course using zinc acetate dihydrate as the zinc precursor[23-24]. The entire process was followed as per our earlier reports[25-27]. Initially, 0.01 M (2.2 g) of $Zn(CH_3COO)_2$ was dissolved in 150 mL of distilled water under constant stirring. To this solution, 25 mL of the neem flower extract was added dropwise and stirred

continuously at room temperature for about 3 h. A gradual change in colour and slight turbidity indicated the formation of ZnO NPs. After the reaction was complete, the mixture was left undisturbed for sedimentation. The precipitate formed was collected, washed and dried in a hot oven at 70°C. The resulting dried powder was calcined at 400°C for 2 h to enhance crystallinity and remove any organic residues. Finally white powder of ZnO NPs was obtained.

Synthesis of ZnS NPs

The zinc chloride ($ZnCl_2$) was used as the zinc basis, and sodium sulfide (Na_2S) served as the sulfur donor. Similarly, 0.01 M (1.36 g) of $ZnCl_2$ was dissolved in 150 mL of distilled water under constant stirring and followed the above process. In a separate beaker, 0.01 M (2.4 g) of Na_2S was dissolved in 100 mL of distilled water and added slowly to the $ZnCl_2$-neem extract mixture under continuous stirring. Upon addition, the reaction mixture turned milky white, indicating the formation of ZnS NPs through a precipitation reaction for an additional 2-3 h to ensure the stabilization. The resulting precipitate was centrifugally collected, dried and stored in airtight containers for further analysis and application.

Characterization techniques

Using Cu-Kα (λ = 0.1542 nm) monochromatic radiation, the structural pattern of the NPs was determined using XRD (X'Pert PRO; Almelo, Netherlands); in the 2θ range from 20° to 80°. An FTIR spectrophotometer was used to record the FTIR spectra in the 400–4000 cm^{-1} range. The functional groups and molecular vibrational characteristics of the NP were determined using the FTIR spectra using an FTIR spectrophotometer (Perkin Elmer, USA). Using a 633 nm laser light source and the DLS concept, the average particle size distribution was calculated using a particle size analyzer (Sympatec, Germany) and the optical absorbance level was assessed using UV-visible spectrophotometer (Cary Agilent, Singapore).

Dye solution preparation

Fresh dye solutions were made in distilled water at a constant dosage of 20 mg/L (20 ppm). The amount of natural photodegradation was determined by exposing 100 mL of each dye solution to sunlight first, without the use of a catalyst. The next series of tests included dispersing the produced NPs in 100 mL of dye solution in separate beakers after adding 100 mg of the NPs under stirring. After that, the suspensions were left in the sun for a certain amount of time to start the photocatalytic breakdown process. The reaction mixtures were sampled every 10 min and examined using a UV-visible spectrophotometer to track any changes in the dyes' signature absorbance peaks[28].

Antibacterial studies

To evaluate the antimicrobial properties of the synthesized ZnO and ZnS NPs, we used the well-diffusion method. The first step was to grow and replicate many bacterial strains in Nutrient Broth for 12 h at 37°C. One common nutritional medium for testing bacteria's resistance is Mueller-Hinton Agar (MHA), which we prepared and then spread out onto sterile Petri plates. After the agar had set, the pre-cultured bacterial suspension was spread out equally across its surface. A sterile borer to fill the agar wells with NP solutions at concentrations of 25, 50, and 100 µg/mL was used. By comparing the samples to chlortetracycline (CT 30), the researchers hoped to standardize their antibacterial effectiveness. The bacteria were able to multiply and interact with the materials after incubating the plates at 37°C for 24 h. The completion of the incubation time allowed us to see the inhibition zones around the wells, indicating that the NPs had effectively halted the development of the bacteria. We measured the size of the zone of inhibition to find out how efficient each sample was against germs.

Results and Discussion

Phase and structural analysis (XRD)

Fig. 1 displays XRD analysis of green-synthesized ZnO and ZnS NPs, including their respective Rietveld refinement plots, which confirm their crystalline structure**,** phase purity, and agreement with standard reference data **(**JCPDS**).** The diffractogram exhibits sharp and intense peaks at 2θ with corresponding planes 31.8° (100), 34.5° (002), 36.3° (101), 47.6° (102), 56.7° (110), 62.9° (103), 66.4° (200), 68° (112), 69.2° (201), 72.6° (004), 77° (202) crystallographic planes of hexagonal wurtzite ZnO[19-20]. The peaks match well with the JCPDS card no. 36-1451, confirming the hexagonal crystal structure. The sharpness and concentration of the peaks indicate that the ZnO NPs are well-crystallized, and no impurity peaks are observed, confirming phase purity. The refinement curve (Fig. 1a) shows excellent agreement between the

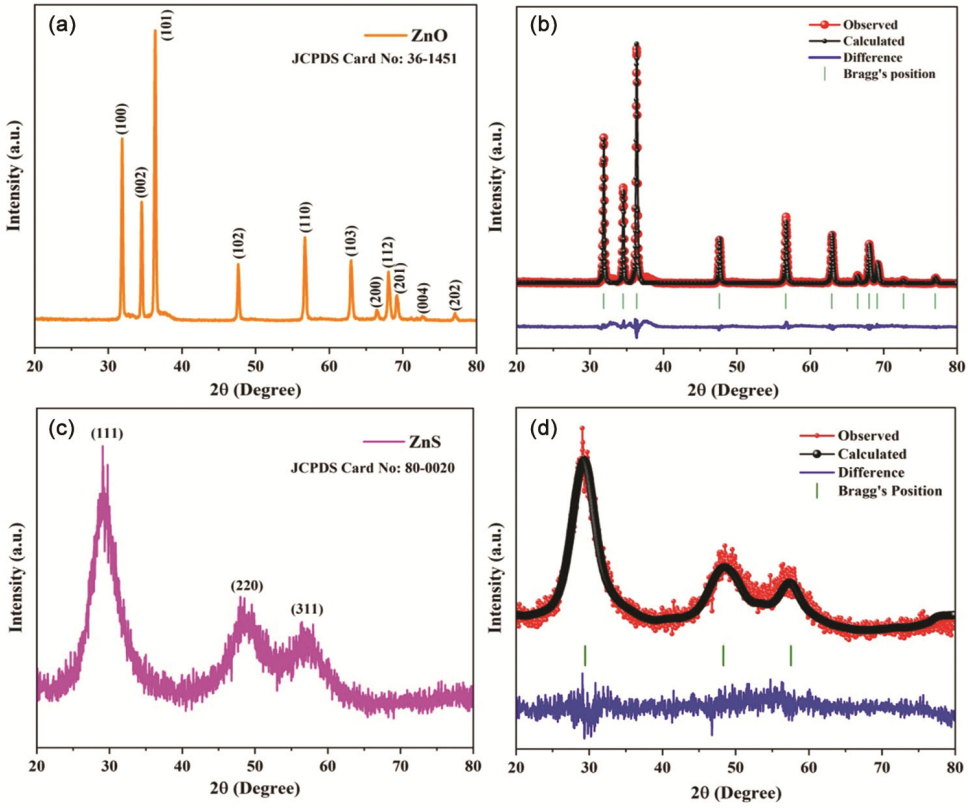

Fig. 1 — XRD images of (a) ZnO, (b) ZnO using refinement, (c) ZnS and (d) ZnS using refinement

Table 1 — XRD structural parameters of prepared samples

Sample	Structure	Lattice parameter (Å)	Space group	Average crystal size (nm)	Dislocation density (lines/nm^2)	Average micro strain (ε) (x 10^{-3})	Rep	Rp	Rwp	Chi^2
ZnO	hexagonal wurtzite	a=b=3.243 c=5.201	*P63mc*	40.42	6.12 x 10^{-4}	3.36	8.47	7.19	13.92	2.73
ZnS	cubic	a=b=c=5.27		16.24	3.79 x 10^{-3}	4.81	15.2	11.44	15.94	1.09

observed and calculated patterns. This confirms that the lattice parameters and crystal structure derived from the green-synthesized ZnO NPs closely match the standard values[21-22].

The low residual error further supports the structural stability and accurate phase formation, as mentioned in Table 1.The ZnS pattern (Fig. 1c) displays broader peaks at 2θ, 29.2°, 48.8°, and 56.8°, equivalent to the (111), (220), and (311) planes of cubic zinc blende ZnS, according to JCPDS. Augmentation of XRD peaks designates the establishment of ZnS nanocrystals. The broadness of the peaks compared to ZnO suggests that the ZnS NPs are smaller or less crystalline. The non-appearance of subordinate peaks designates the pure concentration of the ZnS phase, and the peak positions confirm the successful formation of the cubic phase[23-24]. The refinement plot (Fig. 1d) for ZnS matches the observed and calculated data well, confirming that the synthesized NPs maintain the expected cubic structure. Though the peaks are broader and less intense, the fit is acceptable, and Bragg's positions align well. This indicated that the ZnS NPs are pure, nanocrystalline, and phase-verified.

Functional group analysis (FTIR)

The FTIR spectra (Fig. 2) exhibit broad peaks at 3400, 1643, and 1632 cm^{-1}, attributed to O–H stretching vibrations, signifying the presence of hydroxyl groups from alcohols or phenolic constituents in the *Azadirachta indica* extract and adsorbed moisture on the NP surface[26]. The bands around 2924, 2861, 2926, and 2858 cm^{-1} correspond to C–H stretching of aliphatic –CH_2 and –CH_3 groups, commonly associated with

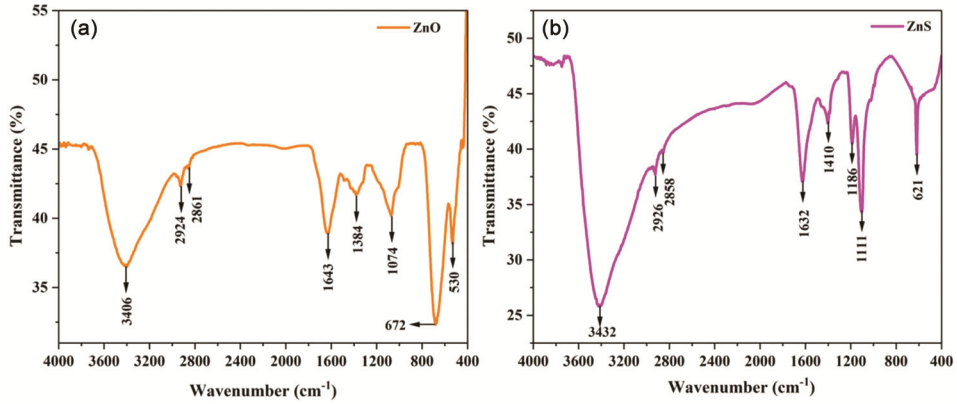

Fig. 2 — FTIR spectra of (a) ZnO and (b) ZnS NPS

flavonoids, terpenoids, and alkaloids, confirming the role of organic molecules as capping and stabilizing agents. The band at 1384 cm^{-1} is assigned to C=O stretching, while those at 1186, 1111, and 1074 cm^{-1} correspond to C-O-C and C-N stretching modes, indicating the presence of ether, amine, and polysaccharide functionalities from phytochemicals. The 1410 cm^{-1} band corresponds to aromatic C=C stretching, characteristic of phenolic and flavonoid compounds[27-28].

Importantly, these phytochemical-derived functional groups particularly hydroxyl (–OH), carbonyl (–C=O), and amine ($–NH_2$) moieties play a crucial role in modulating the surface charge of the synthesized NPs. The oxygen- and nitrogen-rich biomolecules can donate lone-pair electrons to metal centers, forming metal–oxygen (M–O) or metal–nitrogen (M–N) coordination bonds that stabilize the NP surface. This capping process also introduces negative surface potential due to deprotonated –OH and $–COO^-$ groups, which enhances colloidal stability through electrostatic repulsion and prevents agglomeration. The surface-bound biomolecules further influence the zeta potential and interfacial charge distribution, which can directly affect the antibacterial and photocatalytic performance of the NPs by controlling interaction with bacterial cell membranes or charged dye molecules[29-30]. Finally, the intense low-frequency peaks at 672 and 530 cm^{-1}, typical of Zn–O stretching vibrations, confirm the successful formation of ZnO NPs. The characteristic band at 621 cm^{-1} corresponds to the Zn–S stretching mode, confirming the formation of ZnS NPs[31].

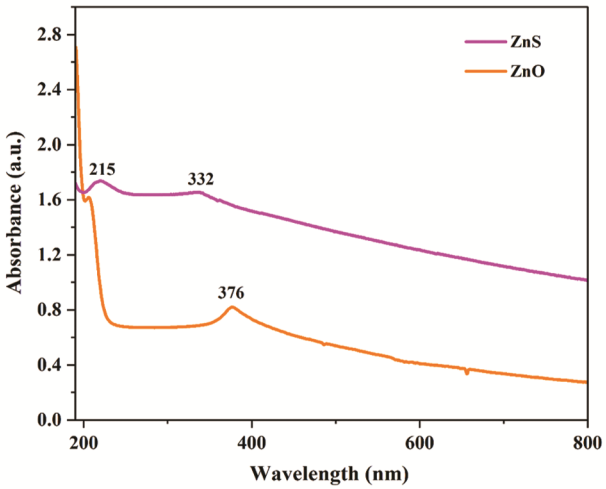

Fig. 3 — Absorption spectra of prepared samples

UV-visible absorption analysis

The absorption spectrum (Fig. 3) of the green-synthesized ZnO reveals a sharp and well-defined peak at around 376 nm, attributed to intrinsic near-band-edge absorption of ZnO. This phenomenon is due to the inherent bandgap absorption, which involves an electronic transition from the oxygen 2p orbitals in the valence band to the zinc 3d orbitals in the conduction band (O 2p → Zn 3d). A typical exciton absorption is blue-shifted for the bulk absorption edge (380 nm). The absorption edge noticeably shifts toward shorter wavelengths or higher energy levels as the NP size decreases, a trend attributed to the quantum confinement effect. This distinct absorption edge indicates the successful formation of crystalline ZnO NPs with relatively uniform size distribution[32-33].

The green-synthesized ZnS display two distinct absorption peaks at 215 nm and another broader peak around 332 nm. The sharp and strong absorption

observed at 215 nm indicates a wide bandgap semiconductor, corresponding to the intrinsic bandgap absorption of ZnS. Compared to bulk ZnS (~340 nm), this blue-shifted absorption suggests the formation of very small NPs, where quantum confinement effects become significant. The secondary peak at around 332 nm may be attributed to surface states or defect-related transitions, often introduced by the organic functional groups in the neem flower extract used during synthesis. The neem flower extract, rich in phytochemicals, reduces zinc ions and stabilizes the formed nanoparticles. These phytochemicals act as reducing and stabilizing agents and adsorb onto the surface of the NPs, introducing structural irregularities or intermediate energy states within the bandgap. These biomolecules also influence the surface states and optical properties, which could further contribute to the tuning of the bandgap[34]. The optical bandgaps of ZnO and ZnS NPs were determined based on their corresponding absorption edge wavelengths. The observed band gap values were 3.30 eV for ZnO and 3.73 eV for ZnS, aligning with previously documented values in the literature for bulk materials, underscoring their characteristics as wide-bandgap semiconductors. Tauc plots were generated using absorption data further to validate the optical bandgap[35]. The optical bandgap values obtained from the Tauc plot were 3.28 eV for ZnO and 3.71 eV for ZnS, which closely correspond with those estimated using the absorption edge method, thereby validating the accuracy of the optical measurements. Minor discrepancies in the methods may arise from variations in experimentation and the sensitivity of measurements. The unique properties of ZnO and ZnS, characterized by their wide bandgap, render them exceptionally appropriate for applications activated by UV light, including photocatalysis, UV photodetectors, and protective coatings. ZnS, possessing a marginally elevated bandgap, demonstrates enhanced transparency in the near-UV spectrum. In contrast, ZnO presents a beneficial blend of UV absorption and charge carrier mobility, rendering it advantageous for various optoelectronic and environmental applications[36].

The size analysis of ZnO and ZnS is depicted in Fig. 4. The average particle size (d_{50}) of the ZnO and ZnS is measured at 85.69 and 24.93 nm, respectively. ZnO exhibits a broader distribution with a peak at 85.69 nm, suggesting a larger average particle size, likely due to the high surface energy and polar nature of ZnO promoting interparticle attraction. In contrast, ZnS shows a narrower distribution at 24.93 nm, indicating better poly-dispersed and smaller size. This may result from rapid nucleation during sulfide formation and the enhanced capping efficiency of plant-derived phytochemicals, which effectively stabilize ZnS NPs[37].

Morphology analysis (FESEM)

From the FESEM image (Fig. 5), the ZnS NPs exhibit aggregated non-spherical structures with irregular clustering. The particles appear to be loosely packed, with non-uniform boundaries. The surface texture is moderately coarse, with visible boundaries between aggregated particles. ZnO nanoparticles exhibit a spherical morphology, appearing more uniform and dispersed than ZnS. At 500 nm, the image (Fig. 5c) shows a more porous and flocculent structure, with larger aggregates and a less uniform distribution of particles. At 100 nm (Fig. 5d) reveals a highly dense and compact arrangement of smaller, more uniform particles. Minimal agglomeration is observed, indicating effective capping by neem extract compounds. This suggests isotropic growth and effective stabilization, likely due to balanced phytochemical interactions on all crystal planes. The histograms of particle size distribution (Fig. 6) corroborate the findings from the FESEM observations.

ZnS NPs exhibit a narrow distribution cantered at 27.2 nm (Fig. 6a), indicating fine, moderately dispersed particles with slight aggregation, consistent with the loosely packed non-spherical characteristics observed in FESEM. In contrast, ZnO displays a broader distribution with a mean size of 96.3 nm (Fig. 6b), which aligns with

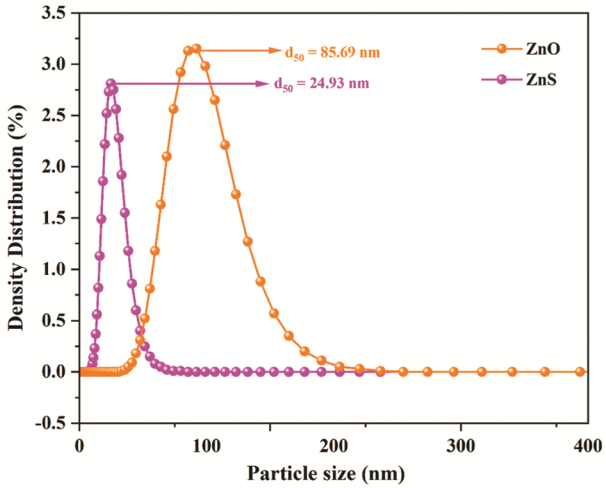

Fig. 4 — PSA of the synthesized samples

the more uniform, compact morphology. The difference results from the unique growth kinetics of phytochemicals in neem extract cap. ZnS surfaces inhibit growth more effectively, while oxide-oxide bonding in ZnO facilitates the formation of larger crystallites. The histogram corroborates nanometer-scale particle sizes, validates the morphological trends identified by FESEM, and supports the findings from XRD and PSA analyses. The elemental analysis from Fig. 7 confirms the presence of synthesized materials. Zinc (Zn) confirms the formation of Zn-based NPs (ZnO/ZnS). Oxygen (O) confirms the strong presence in ZnO samples and the oxide phase. Sulphur (S) detected in ZnS samples confirms sulfide formation with 26.18 wt.%. The successful detection of Zn, O (for ZnO) and Zn, S (for ZnS) validates the formation of desired NPs.

Dye degradation behaviour

The degradation of hazardous dye pollutants, specifically acrylic orange and alizarin red S, are commonly found in textile industry wastewater and are particularly problematic due to their complex aromatic structures, high stability, and resistance to biodegradation.

Acrylic orange dye exhibits a maximum absorbance peak of around 483 nm, while alizarin red S shows its peak absorbance at approximately 425 nm. During photocatalytic analysis, the degradation of these dyes were monitored by recording the decrease in their

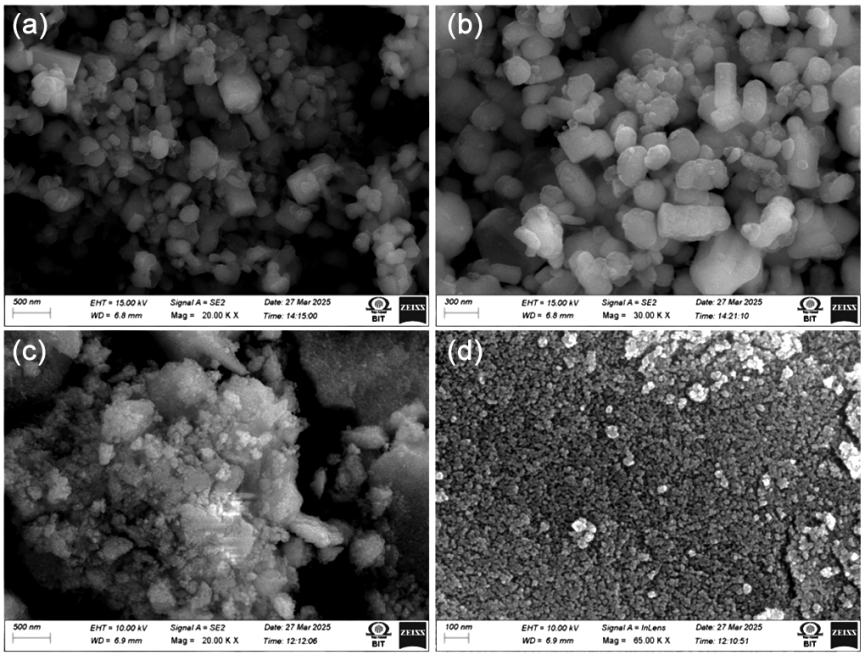

Fig. 5 — FESEM images of (a & b) ZnS NPs and (c & d) ZnO NPs

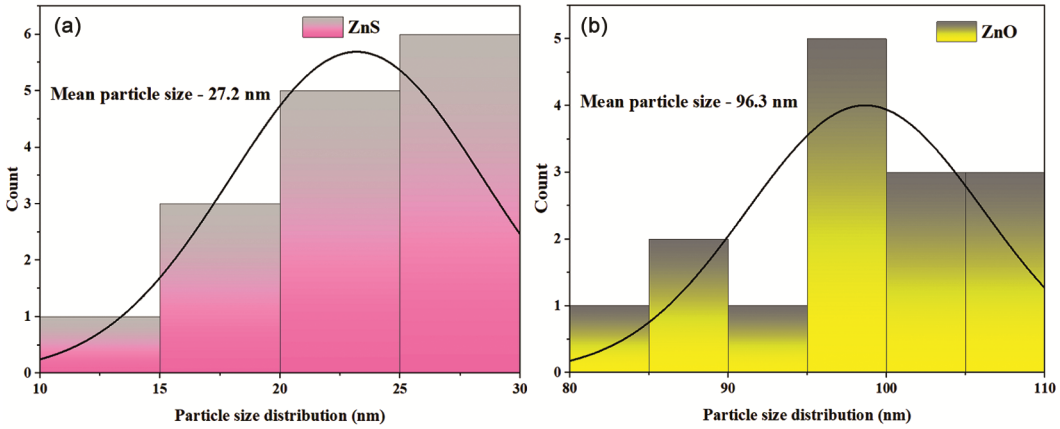

Fig. 6 — Histograms of (a) ZnS and (b) ZnO NPs

respective absorbance intensities over time under sunlight exposure. The disappearance of these characteristic peaks indicates the breakdown of the dye molecules, confirming the photocatalytic efficiency of the synthesized nanomaterials. Fig. 8 displays the dye absorbance graph with a time interval

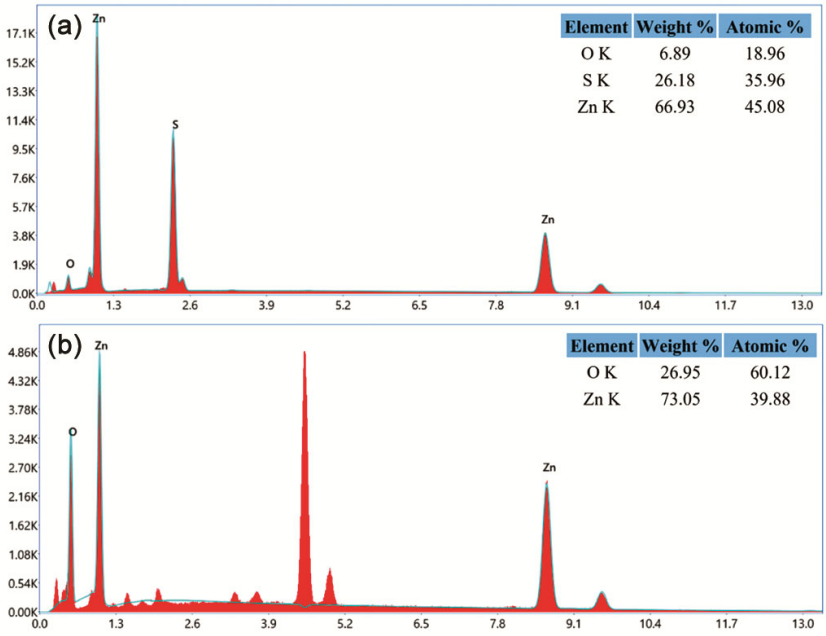

Fig. 7 — EDX images of (a) ZnS and (b) ZnO nanoparticles

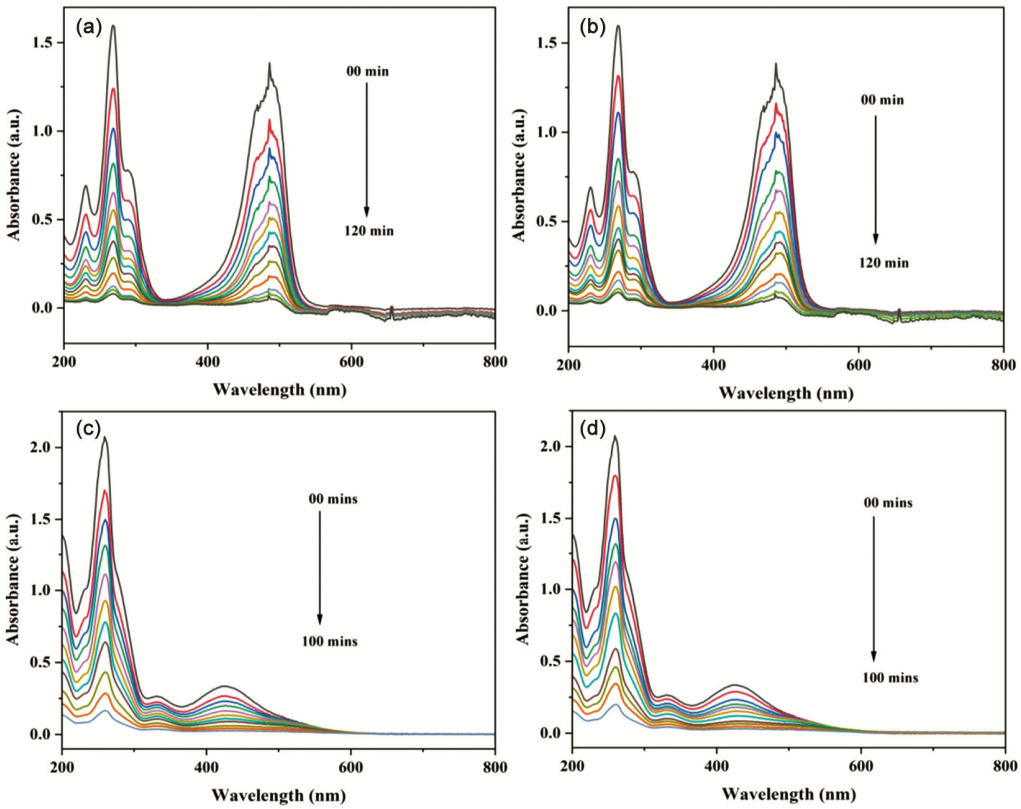

Fig. 8 — Absorbance spectra recorded with time for degradation of Acrylic orange dye using (a) ZnO, (b) ZnS and for degradation of Alizarin red S dye using (c) ZnO & (d) ZnS

of 10 min. Upon exposure to light, electrons (e^-) transition from the valence band (VB) to the conduction band (CB), consequential in the establishment of holes (h^+) in the VB. The charge carriers subsequently move to the surface and engage in redox reactions which are powerful oxidants that non-selectively degrade dye molecules into less harmful or mineralized end-products like CO_2 and H_2O[21-23].

Dye degradation efficiency

Fig. 9 presents the synthesized samples with respective dyes, the C/C_0 graph (a & b), and the dye degradation efficiency graph (c & d). The percentage degradation efficiency of the dyes was calculated using the formula[38]:

$$\text{Degradation Efficiency (\%)} = 1 - \frac{C_t}{C_0} \times 100 \quad \ldots (1)$$

The C_0 is the initial absorbance, and C_t is the absorbance at time t. It was visually observed that the dye solution gradually turned colourless due to the photodegradation of dyes. The degradation proceeds, where the chromophoric groups such as azo (-N=N-), hydroxyl (-OH), and aromatic rings in acrylic orange and alizarin red S dyes are broken down. The cleavage of these bonds leads to the destruction of the conjugated π-electron systems, resulting in the loss of colour and the formation of low-molecular-weight, non-toxic end products such as CO_2, H_2O, and other small organic acids. ZnO exhibited a slightly higher degradation efficiency for both dyes compared to ZnS. At 120 min of radiation, ZnO achieved 95.72% degradation for acrylic orange, while ZnS reached 94.07%. Similarly, at 100 min of radiation, ZnO showed 92.37% for alizarin red S, and ZnS had 90.97% degradation. The slightly better performance of ZnO can be attributed to its higher crystallinity, better charge separation, and stronger oxidative potential. Additionally, ZnO's narrower bandgap (~3.3 eV) compared to ZnS allows more efficient light absorption under visible light irradiation, enhancing photocatalytic activity[26-27]. The spherical morphology of ZnO and slightly irregular structures in ZnS influence the efficiency by affecting light scattering and surface interaction. The presence of phytochemicals from neem extract also enhances the surface reactivity and stabilizes the NPs, further contributing to efficient dye degradation[28-30].

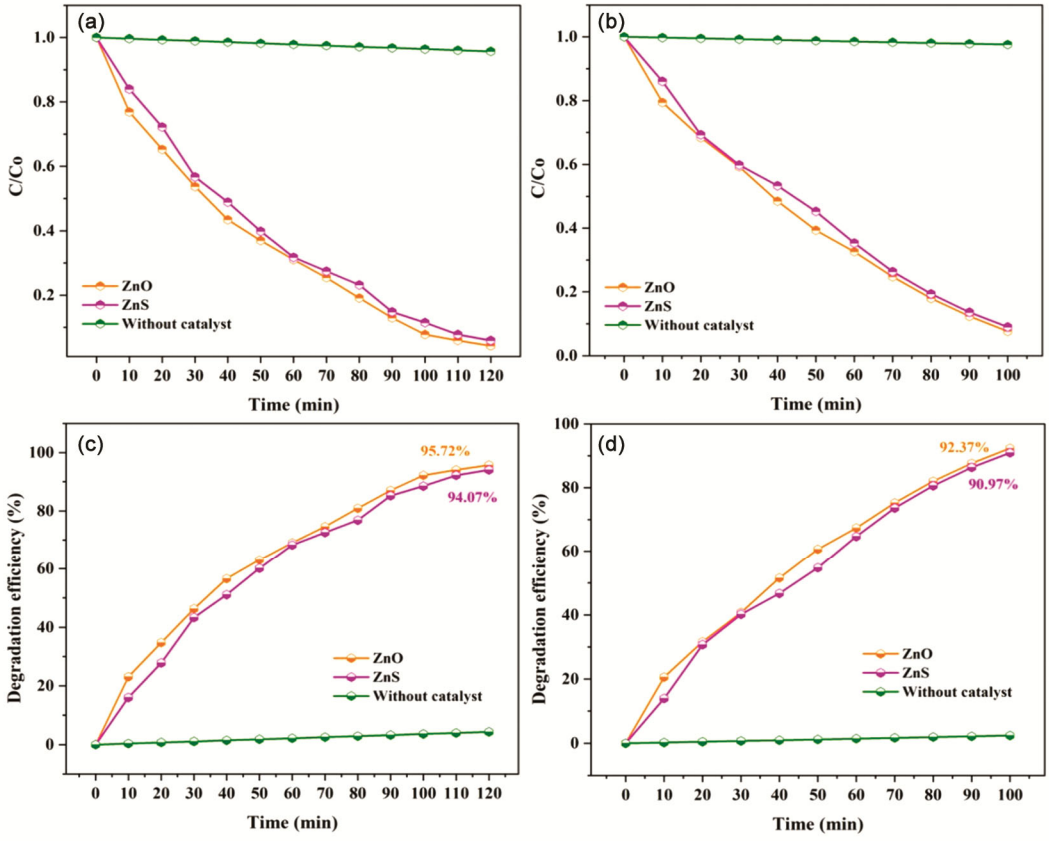

Fig. 9 — (a) & (b) C/C_0 graph and (c) & (d) degradation efficiency graphs for acrylic orange dye and alizarin red S dye

Pseudo-first-order kinetics

The pseudo-first-order kinetics graph is presented in Fig. 10. The degradation kinetics equation (Eq. 2), was used for the determination of the reaction's pseudo-first-order kinetics and kinetic constant[39].

$$In\frac{C}{C_0} = kt \quad \ldots (2)$$

ZnO exhibited a higher rate constant (2.555 x10^{-2} min^{-1} for acrylic orange and 2.3947 x10^{-2} min^{-1} for alizarin red S) than ZnS (2.3123 x10^{-2} min^{-1} for acrylic orange and 2.3087 x10^{-2} min^{-1} for alizarin red S), indicating faster reaction rates. Slightly lower rate constants for degradation of alizarin red S in both catalysts suggest that this dye is more structurally complex and less readily degradable than acrylic orange due to its anthraquinone structure, which is more resistant to oxidative attack. Table 2 summarizes the photocatalytic results obtained for ZnO and ZnS NPs.

Stability and reusability

For acrylic orange dye degradation, the proportion loss in photocatalytic effectiveness after 5 cycles was detected to be 88.22% for ZnO and 87.97% for ZnS, respectively (Fig. 11). Similarly for alizarin red S dye

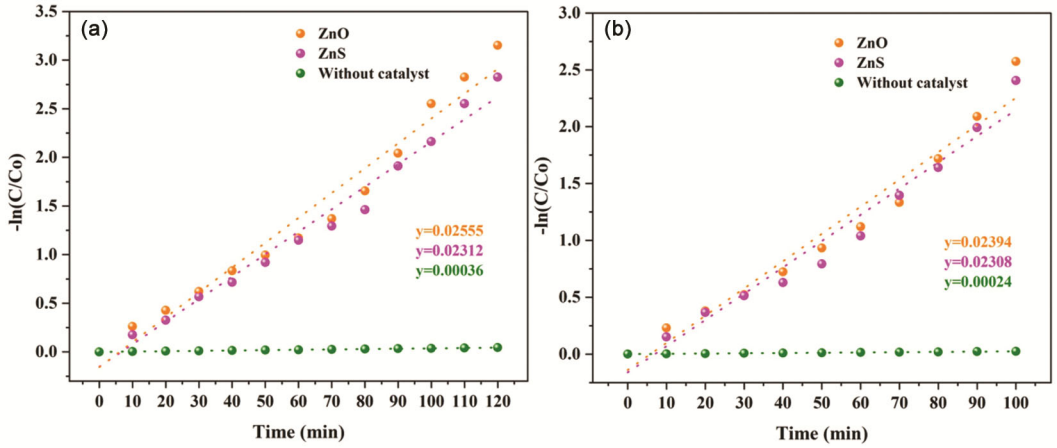

Fig. 10 — Pseudo-first order kinetics graphs for (a) acrylic orange dye and (b) alizarin red S dye degradation

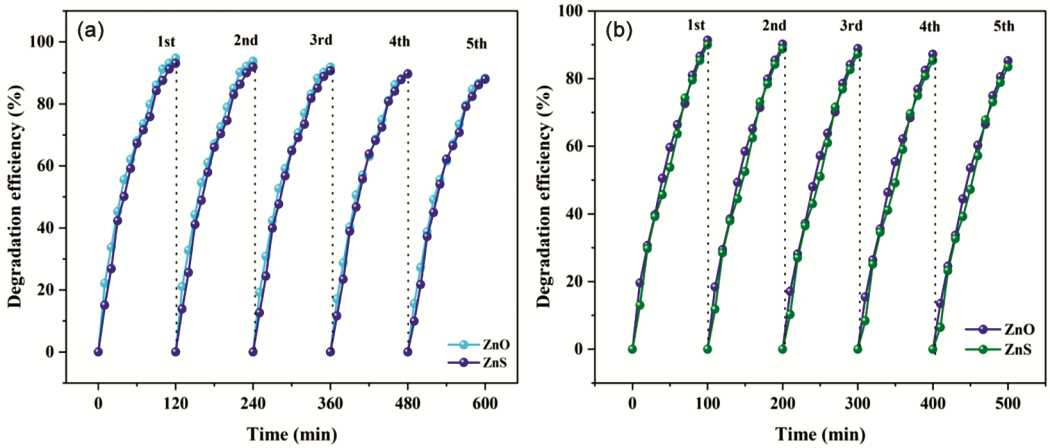

Fig. 11 — Recycle stability efficiency graph for (a) acrylic orange dye and (b) alizarin red S dyes

Table 2 — Nanocatalyst with kinetic rate constant and degradation efficiency

Sample	Dye used	Irradiation time (min)	Degradation efficiency (%)	Rate constant (x10^{-2} min^{-1})	Stability after 5 cycles (%)
ZnO	Acrylic orange	120	95.72	2.555	88.22
	Alizarin red S	100	92.37	2.3947	85.26
ZnS	Acrylic orange	120	94.07	2.3123	87.97
	Alizarin red S	100	90.97	2.3087	83.45

degradation, with efficiency loss of 85.26% for ZnO and 83.45% for ZnS. Both ZnO and ZnS demonstrated good reusability after five photocatalytic cycles. The slight decline in activity may be due to photocorrosion, surface fouling by dye intermediates, or agglomeration during repeated use. ZnO showed marginally better stability, likely due to its more robust structure and lower tendency to undergo photo-dissolution than ZnS[39-40]. The photocatalytic schematic mechanism has been presented in Fig. 12.

Antibacterial behaviour

The green-synthesized ZnO and ZnS NPs also exhibited promising antibacterial activity (Fig. 13), particularly against *Staphylococcus aureus* and *Escherichia coli* bacterial strains. The results revealed that the inhibition zone was consistently larger for *S. aureus* (16.9 mm) compared to *E. coli (15.5 mm)*, indicating that these NPs are more effective against gram-positive bacteria. Hence, ZnS also shows higher activity against *S. aureus* (16.1 mm) than *E. coli* (14.9 mm). However, ZnS generally generates lower quantities of ROS than ZnO, which correlates with our results slightly reduced antibacterial performance. *S. aureus* possesses a thick but relatively porous peptidoglycan layer without an outer membrane, which allows easier penetration and interaction of NPs and ROS. In contrast, *E. coli* has a more complex cell wall structure with a thin peptidoglycan layer shielded by an outer membrane composed of lipopolysaccharides, which acts as a barrier, limiting nanoparticle entry and ROS diffusion[32-35]. Fig. 14 presents a graphic picture of the antibacterial mechanism.

The antibacterial mechanism of ZnO and ZnS NPs involves multiple pathways and the reactive species damage the bacterial cell wall, disrupt membrane integrity, and oxidize essential biomolecules, leading to cell death[21-24]. Additionally, the Zn^{2+} ions released from the NPs may interfere with enzymatic activity and metabolic pathways, further enhancing antimicrobial efficacy. Moreover, using neem flower extract in the

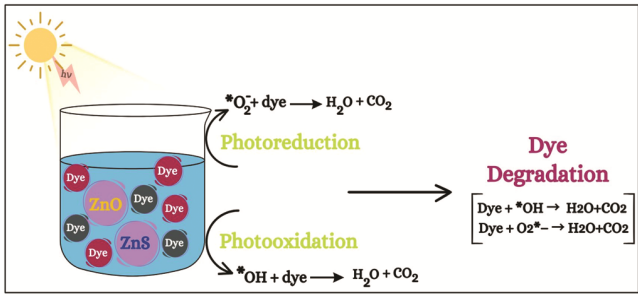

Fig. 12 — Degradation mechanism of prepared photocatalyst

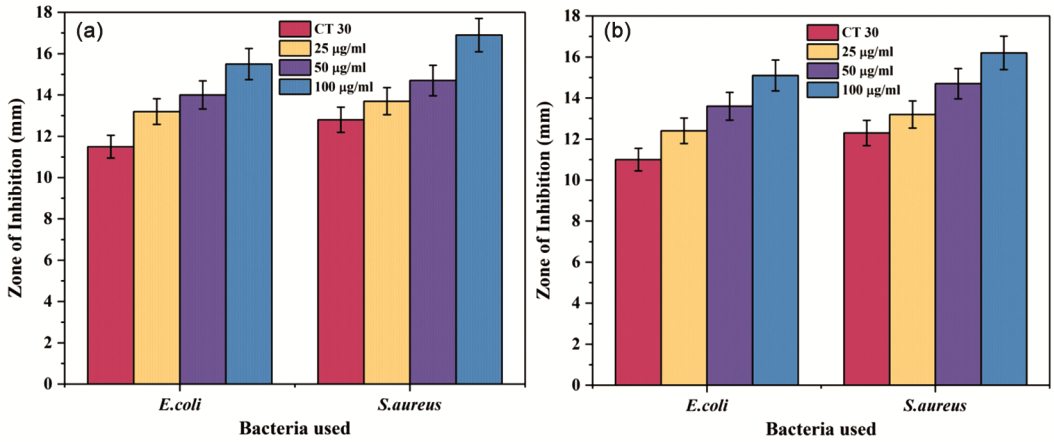

Fig. 13 — Plots for antibacterial efficiencies of (a) ZnO and (b) ZnS

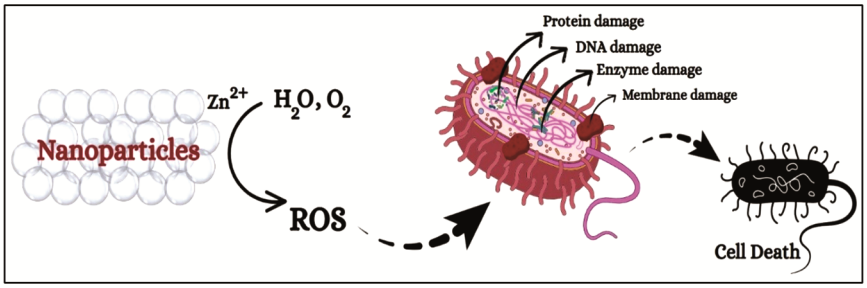

Fig. 14 — Graphical representation of the antibacterial mechanism

synthesis enhances the antimicrobial activity. The phytochemicals from neem, such as flavonoids, terpenoids, and alkaloids, may remain attached to the nanoparticle surface, contributing synergistically to bacterial inhibition through their antimicrobial properties[29-30]. Improved bactericidal effectiveness is a result of the reduced size and increased surface area of the NPs, which allow for greater contact with bacterial membranes and ROS generation[35-37].

Conclusion

ZnO and ZnS nanoparticles were synthesized using a green synthesis route employing neem flower extract as a natural reducing and stabilizing agent. This environmentally friendly approach eliminated harmful chemicals and efficiently produced multifunctional nanomaterials under mild conditions. The XRD results confirmed the formation of hexagonal wurtzite ZnO and cubic ZnS structures. The calculated average crystallite sizes were 40.42 nm for ZnO and 16.24 nm for ZnS. FTIR analysis validated the presence of phytochemical capping from neem extract, which provided stability and may have influenced the growth direction of the particles. UV-visible absorption spectra revealed strong absorption peaks at 376 nm for ZnO and 215 and 332 nm for ZnS**,** with estimated bandgaps of 3.30 eV (ZnO) and 3.71 eV (ZnS)**,** supporting the quantum confinement effect. Morphological observations through FESEM showed that ZnO possessed a spherical and more uniform morphology, while ZnS was irregular and flaky, influencing their functional behaviour. These structural differences are strongly influenced by the interaction of the metal precursors with biomolecules present in neem extract. In photocatalytic studies, both nanoparticles demonstrated high dye degradation capabilities under sunlight. ZnO achieved slightly higher degradation percentages (95.72 and 94.07%) and faster reaction kinetics (2.555 and 2.312 x 10^{-2} min^{-1}), likely due to its larger crystallite size and enhanced light absorption, which promoted the efficient generation of charge carriers. Stability tests over five cycles showed minimal loss in activity for both materials, confirming their practical reusability. The antibacterial evaluation revealed significant inhibitory effects against *S. aureus* and *E. coli*, with ZnO showing broader inhibition zones. This superior antibacterial action is attributed to a synergistic effect of ROS generation, Zn^{2+} ion release, and bio-functionalized surfaces from the neem extract.

Conflict of interest

The authors declare no conflict of interest.

References

1 Mustafa B M & Hassan N E, Water contamination and its effects on human health: A review, *Environ Earth Sci Int*, 28 (2024) 38.

2 Sharma A, Grewal A S, Sharma D & Srivastav A L, Heavy metal contamination in water: Consequences on human health and environment, *Metals Water*, 30 (2023) 772.

3 Lin L, Yang H & Xu X, Effects of water pollution on human health and disease heterogeneity: A review, *Front Environ Sci*, 10 (2022) 46.

4 Getahun Y W, Manciu F S, Li X & El-Gendy A A, Green synthesized super paramagnetic iron oxide nanoparticles for water treatment, *J Mol Liq*, 356 (2022) 118983.

5 Anindita N B, Singh M, Guin S & Barthwal M, Current Pharmaceutical Biotechnology, *Bentham Science Publishers*, 24 (2023) 101.

6 Nasrollahzadeh M, Sajjadi M, Iravani S & Varma R S, Green-synthesized nanocatalysts and nanomaterials for water treatment: Current challenges and future perspectives, *J Hazard Mater*, 401 (2021) 123401.

7 Bognar S, Putnik P & Sojic D, Sustainable green nanotechnologies for innovative purifications of water: Synthesis of the nanoparticles from renewable sources, *Nanomaterials*, 12 (2022) 263.

8 Hussain R T, Hossain M S & Shariffuddin J H, Green synthesis and photocatalytic applications of zinc oxide nanoparticles (ZnO NPs) for wastewater treatment, *Mater Today Sustain*, 26 (2024) 100764.

9 Bhattacharjee N, Som I, Saha R & Mondal S, A critical review on novel eco-friendly green approach to synthesize zinc oxide nanoparticles for photocatalytic degradation of water pollutants, *Int J Environ Anal Chem*, 104 (2024) 489.

10 Munyai S & Hintsho-Mbita N C, Green derived metal sulphides as photocatalysts for waste water treatment-A review, *Curr Res Green Sustain Chem*, 4 (2021) 100163.

11 Sarangi B, Mishra S P & Behera N, Advances in green synthesis of ZnS nanoparticles: An overview, *Mater Sci Semicond Process*, 147 (2022) 106723.

12 Bai X, Chen W, Wang B, Sun T, Wu B & Wang Y, Photocatalytic degradation of some typical antibiotics: Recent advances and future outlooks, *Int J Mol Sci*, 23 (2022) 8130.

13 Ruziwa D T, Oluwalana A E, Mupa M, Sillanpaa M, Gwenzi W & Chaukura N J, Remediation strategies of antiretroviral drugs in the aquatic environment: Current trend and future perspectives, *Water Proc Eng*, 54 (2023) 103880.

14 Velempini T, Prabakaran E & Pillay K, Recent developments in the use of metal oxides for photocatalytic degradation of pharmaceutical pollutants in water-A review, *Mater Today Chem*, 19 (2021) 100380.

15 Gudkov S V, Burmistrov D E, Serov D A, Rebezov M B & Lisitsyn A B, A mini review of antibacterial properties of ZnO nanoparticles, *Front Phys*, 9 (2021) 44.

16 Kalra K, Chhabra V & Prasad N, Antibacterial activities of zinc oxide nanoparticles: A mini review, *J Phys Conf Ser*, 2267 (2022) 012049.

17 Sharma D K, Shukla S, Sharma K K & Kumar V, A review on ZnO: Fundamental properties and applications, *Mater Today*, 49 (2022) 3028.

18 Pandey P & Choubey A K, Green synthesized ZnO@CuO nanocomposites using Achyranthes aspera leaves extract for dielectric applications, *J Alloys Compd*, 970 (2024) 172492.

19 Mousa S A, Wissa D A & Khairy S A, Enhanced photocatalytic activity of green synthesized zinc oxide nanoparticles using low-cost plant extracts, *Sci Rep*, 14 (2024) 16713.

20 El-Khawaga A M, Elsayed M A, Hashem A H, Zaher A A, Mohsen M & Salem S S, Green synthesized ZnO nanoparticles by Saccharomyces cerevisiae and their antibacterial activity and photocatalytic degradation, *Biorefin*, 15 (2025) 2673.

21 Flores B, Guzman M, Chumpitaz O & Herrera E, Crystallographic and optical properties of ZnO nanoparticles prepared by two different methods, *Appl Phys A Mater Sci Process*, 131 (2025) 300.

22 Donia D, Bauer E, Tagliatesta P, Gontrani L & Carbone M, Room temperature syntheses of ZnO and their structures, *Symmetry*,13 (2021) 733.

23 Kannan S, Subiramaniyam N P & Sathishkumar M, Green synthesized zinc sulfide nanoparticles from Tridax procumbens plant extract for improved photocatalytic activity, *Mater Today*, 51 (2022) 1727.

24 Thomas S A, Kadam S A, Ma Y R & Aravind A, Rational design of selenium inserted 1T/2H mixed-phase molybdenum disulfide for energy storage and pollutant degradation applications, *Chem Select*, 6 (2021) 10015.

25 Tamanna N, Hossain M, Bahadur N & Ahmed S, Green synthesis of Ag_2O & facile synthesis of ZnO and characterization using FTIR, bandgap energy & XRD (Scherrer equation, Williamson-Hall, Size-train plot, Monshi-Scherrer model), *Results Chem*, 7 (2024) 101313.

26 Ayodhya D & Veerabhadram G J, Green synthesis, optical, structural, photocatalytic, fluorescence quenching and degradation studies of ZnS nanoparticles, *Fluorescence*, 26 (2016) 2165.

27 Munyai S, Mahlaule-Glory L M & Hintsho-Mbita N C, Green synthesis of Zinc sulphide (ZnS) nanostructures using S. frutescences plant extract for photocatalytic degradation of dyes and antibiotics, *Mater Res Exp*, 9 (2022) 015001.

28 Reddy P L, Deshmukh K, Chidambaram K, Lakshmipathy R & Pasha S K K, Dielectric properties of polyvinyl alcohol (PVA) nanocomposites filled with green synthesized zinc sulphide (ZnS) nanoparticles, *J Mater Sci: Mater Electron*, 30 (2019) 4676.

29 Fakhari S, Jamzad M & Kabiri F H, Green synthesis of zinc oxide nanoparticles: A comparison, *Green Chem Lett Rev*, 12 (2019) 19.

30 Khan M M, Kumar S, Ahamed M, Al-Khedhairy A A & Musarrat J, Green synthesis, structural and optical characterization of zinc oxide nanoparticles and evaluation of their antimicrobial activity, *Mater Res Bull*, 48 (2013) 3243.

31 Upadhyaya H, Shome S, Sarma R, Tewari S, Bhattacharya M K & Panda S K, American, green synthesis, characterization and antibacterial activity of ZnO nanoparticles, *J Plant Sci*, 9 (2018) 1279.

32 Samy A, El-Sherbiny A E & Menazea A A, Green synthesis of high impact zinc oxide nanoparticles, *Egypt J Chem*, 62 (2019) 29.

33 Renuka D, Praveena B, Pourkodee D & Sivanesan T, Effective facile green route for the synthesis of stabilized ZnS nanoparticle: Compact discussion on structural, optical, photocatalytic degradation performance for picric acid under UV-Visible light, *Mater Today*, 68 (2022) 586.

34 Johar M A, Afzal R A, Alazba A A & Manzoor U, Photocatalysis and bandgap engineering using ZnO nanocomposites, *Adv Mater Sci Eng*, 2015 (2015) 1.

35 Chen X, Wu Z, Liu D & Gao Z, Preparation of ZnO photocatalyst for the efficient and rapid photocatalytic degradation of azo dyes, *Nanoscale Res Lett*, 12 (2017) 143.

36 Sharma M, Jain T, Singh S & Pandey O P, Photocatalytic degradation of organic dyes under UV-visible light using capped ZnS nanoparticles, *Solar Energy*, 86 (2012) 626.

37 Lee G J & Wu J J, Shell layer thickness-dependent photocatalytic activity of ZnO-ZnS core-shell nanorods, *Powder Technol*, 318 (2017) 8.

38 Abebe B, Zereffa E A, Tadesse A & Murthy H C A, A review on enhancing the antibacterial activity of ZnO: Mechanisms and microscopic investigation, *Nanoscale Res Lett*, 15 (2020) 190.

39 He W, Zheng Z, Wamer W G & Yin J J, Bandgap-engineered ZnS quantum dots and their size-dependent reactive oxygen species generation, *J Phys Chem C Nanomater Interf*, 120 (2016) 3187.

40 Hojamberdiev M, Piccirillo C, Cai Y, Kadirova Z C, Yubuta K & Ruzimuradov O, ZnS-containing industrial waste: Antibacterial activity and effects of thermal treatment temperature and atmosphere on photocatalytic activity, *J Alloys Compd*, 791 (2019) 971.